A High-Efficiency High-Density Three-Phase *CLLC* Resonant Converter With a Universally Derived Three-Phase Integrated Transformer for On-Board-Charger Application

Feng Jin, *Graduate Student Member, IEEE*, Ahmed Nabih, *Member, IEEE*, Tianlong Yuan, *Graduate Student Member, IEEE*, and Qiang Li, *Member, IEEE*

***Abstract*—This article proposed a universal method of integrating magnetizing inductance with built-in leakage inductance based on multiple perfectly coupled transformers (PCTs). The integration of built-in leakage inductance can be achieved by connecting several PCTs using a standardized core type for cost considerations or can be further integrated into a customized core with interleaved magnetomotive force polarities across transformer legs to achieve better flux distribution and smaller core loss. The proposed concept can be applied to single-input single-output and multiple-input multiple-output integrated transformer applications. A 3 × 3 PCTs based integrated transformer built with printed circuit board windings was designed for a three-phase *CLLC* (3 PCLLC) resonant converter, which integrates three primary resonant inductors, three secondary resonant inductors, and three transformers into one magnetic core to simplify the complexity of the converter. The effectiveness of the proposed concept was demonstrated through a high-efficiency, high-power density 3 PCLLC dc/dc converter for an 800-V 16.5-kW on-board charger. The designed converter can achieve a power density of 500 W/in^3 and a peak efficiency of 98.8%.**

***Index Terms*—Built-in leakage inductance, *CLLC*, magnetic integration, on-board charger (OBC), printed circuit board (PCB) transformer, three-phase.**

I. Introduction

ELECTRIC vehicles (EVs) can play a pivotal role in achieving zero emissions by 2050, aligning with the ambitious environmental goals set by numerous countries worldwide. Governments around the globe are actively formulating plans and policies to accelerate the transition from gas-driven cars to EVs [1], [2], [3]. These initiatives demonstrate the commitment of governments worldwide to reduce greenhouse gas emissions and combat climate change by phasing out gas-driven cars. By promoting the adoption of EVs through incentives, infrastructure development, and regulatory measures, countries are paving the way for a sustainable and clean transportation future. Based on the data in [4], the EV market is growing very fast and will increase by 100% in 2027 over 2023, so are the charging stations to meet the upcoming charging demand for EVs.

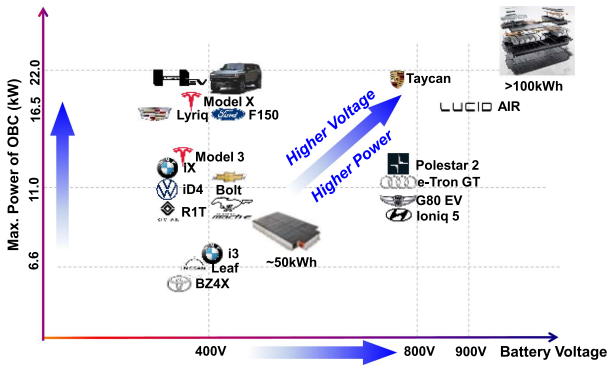

Fig. 1. Battery pack design and its on-board-charger power level in state-of-the-art EVs.

There are two ways of charging methods to refill the battery pack inside the EVs: on-board charger (OBC) and off-board charger (fast charger). In the state-of-the-art EV markets, some of their battery pack design and equipped OBCs are shown in Fig. 1. The horizontal axis is the nominal battery voltage for a battery pack design inside the EVs and the vertical axis is the output power level of the equipped OBCs. In today's EV market, most EVs adopt 400 V battery pack with 6.6 kW OBC or 11 kW OBC for a larger capacity battery pack. Some large SUVs or trunk that use larger battery packs will be equipped with 16.5 kW and 19.2 kW OBC, which is limited by the voltage and current rating for household applications. The output power rating of OBC is increasing. Some EV manufacturers shift to the 800 V battery pack design to reduce the total system cost and enable higher fast charging capability, such as Porsche Taycan and Audi e-Tron GT. The Lucid Air EV takes things a step further with 900 V architecture. The EVs' battery voltage and OBC are moving toward higher voltage and higher power as a

Manuscript received 21 September 2023; revised 16 November 2023 and 29 December 2023; accepted 12 January 2024. Date of publication 16 January 2024; date of current version 16 February 2024. This work was supported by the Power Management Consortium in CPES, Virginia Tech. Recommended for publication by Associate Editor O. Lucia. *(Corresponding author: Qiang Li.)*

Feng Jin, Tianlong Yuan, and Qiang Li are with the Center for Power Electronics Systems, Virginia Polytechnic Institute and State University, Blacksburg, VA 24061-0131 USA (e-mail: fengjin@vt.edu; tianlong@vt.edu; lqvt@vt.edu).

Ahmed Nabih is with Texas Instruments, Inc., Dallas, TX 75243 USA (e-mail: nabih@vt.edu).

Color versions of one or more figures in this article are available at https://doi.org/10.1109/TPEL.2024.3354679.

Digital Object Identifier 10.1109/TPEL.2024.3354679

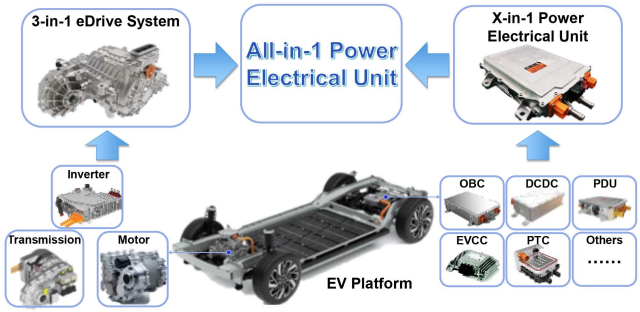

Fig. 2. High-voltage parts integration inside EVs.

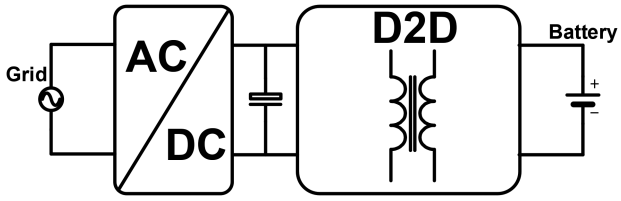

Fig. 3. Two-stage structure of OBC.

larger capacity battery (over 100 kWh) is installed inside. To summarize, there are three trends in the design of battery pack and its OBC of state-of-the-art EVs.

1) The 800 V battery pack design to enhance fast charging capability and improve performance.
2) Larger battery pack design with over 100 kWh to increase the mile range in every charging cycle.
3) The larger output power of OBC to shorten the charging time.

For household applications, EV users can charge their battery pack through OBC inside the EV, which is grid-to-vehicle energy transfer. When necessary, the EV can provide energy to the household appliances or to the grid, which is the vehicle-to-grid energy transfer for emergency use or meet the upcoming demand of smart grid function. The OBC should be bidirectional.

In an EV, such as traditional automobiles, system reliability is crucial. An integrated powertrain architecture is more reliable because fewer parts can break. Outside of the inherent advantages of an integrated system, ensuring reliability in the high-voltage battery environment of an EV also requires robust protection and peak thermal performance. The automanufacturers prefer the integration of motors, transmission, and inverter to form a 3-in-1 eDrive system and try to integrate power electrical units, such as OBC, direct current direct current (DCDC), power distribution unit (PDU), and positive temperature coefficient (PTC) heaters, into an *x*-in-1 power electronic unit. Further integration can be achieved by integrating both above-mentioned high-voltage parts into an all-in-1 power electrical unit, as shown in Fig. 2. Thus, the manufacture of an EV can be much easier, as fewer components are installed inside the EV, and better performance can be achieved due to the reduced weight and volume. This brings new challenges to the OBC: high power density, high efficiency, and bidirectional energy transfer.

Although single-stage ac-to-dc solutions seem to be simpler and more appealing, it has several drawbacks that limit their wide applicability, such as non-zero-voltage switching (ZVS) for ac-side switches and lower overall system efficiency due to wide operation range, more energy storage elements to absorb the double-line-frequency ripple power [5]. Alternatively, a two-stage structure, as shown in Fig. 3, can be adopted: a nonisolated power factor correction (PFC) ac/dc converter can be series connected with a dc/dc converter providing voltage regulation and isolation capability as the second stage. Many research works have been presented with this two-stage solution [6], [7], [8], [9], [10].

For the single-phase ac/dc stage, the bridgeless totem-pole PFC shows great potential due to its simplicity, a smaller number of components, and soft-switching capability when working at critical conduction mode (CRM) and bidirectional energy transfer [11], [12] over the conventional boost PFC running at continuous conduction mode (CCM). For the three-phase ac/dc stage, the Vienna rectifier [13], three-phase buck–boost current dc-link PFC rectifier [14], and two-channel interleaved three-phase ac–dc converters with critical conduction mode [15] are good candidates for bidirectional energy transfer.

The dc transformer is an effective topology for high efficiency [16], [17]. Nonetheless, it possesses a restricted gain range because of its inherent characteristics. An additional stage will be required to achieve wide output voltage regulation and mitigate double-line-frequency ripple with the increased cost and sacrificed power density. The dc/dc converter with regulation capability will be preferred for the second stage, as shown in Fig. 3, based on the cost and power density considerations. Dual active bridge (DAB) [18], [19] or *CLLC* converter [6], [20], [21], [22], [23], [24], [25] are good topology candidates for bidirectional applications over *LLC* [26], [27], [28], [41] converter as they have a symmetrical voltage gain range. The turn-OFF current of the DAB converter is relatively larger than the *CLLC* resonant converter, resulting in a more considerable turn-OFF loss and lower expected efficiency. However, the *CLLC* resonant converters require inductors on both sides of the transformer, which results in more complex circuits and higher costs. Magnetic integration can be a promising technology in simplifying the circuits and reducing the converter's cost [20], [21], [22], [27], [28], [29], [30], [31], [32], [33], [34], [35], [36], [37], [38], [39], [40], [41], [42]. The key to integrating leakage inductance is to make the flux generated by the windings of one side not fully linked with the other side of the transformer so that the primary and secondary windings are not perfectly coupled.

For integrated transformers with little built-in leakage inductance, several transformers with the same turn ratio between primary and secondary windings are integrated into one component to achieve evenly distributed flux by controlling the flux direction in each transformer's core leg [27], which can achieve smaller size and core loss for the transformers. In [28], a high leakage inductance value is achieved by wrapping the primary winding around an additional UI core to serve as a series inductor on the transformer's primary side. In [29], a matrix transformer and matrix inductor were proposed by adopting inductor core

legs and transformer core legs with much-improved flux distribution and smaller core loss. This approach uses extra cores to confine the leakage flux and integrated inductance. However, this integration method demands more space for magnetic components, compromising the magnetic structure's power density. Moreover, additional cores are needed to introduce built-in leakage inductance on the secondary side, which further increases space requirements and diminishes power density.

An alternative approach to incorporating leakage inductance into the transformer involves adjusting the physical distance between the primary and secondary windings using a specialized bobbin design [30], [31]. This method is straightforward but comes at the expense of increased winding losses due to the absence of interleaving between primary and secondary windings. In addition, the leakage flux leaks from the magnetic core, potentially causing interference with nearby components and circuits.

To keep the leakage flux within the core, adding a ferrite core leg with an air gap or using a core leg made of low permeability magnetic material, particularly in an EI core, can be beneficial [32], [33]. The reluctance of the added core leg can be used to adjust the flux distribution inside the core and ensure that the flux from the primary windings will not be fully linked with the secondary windings. The concept, as presented in [32], was adopted and extended to an integrated transformer that utilizes a printed circuit board (PCB) board with an EI-core structure [21]. The primary and secondary windings are not perfectly interleaved and are placed across the outer two legs of the EI core, where the middle leg can serve as the low-reluctance path for the leakage flux. The air gap reluctance of the middle leg can be adjusted to control the leakage inductance of the integrated transformer. Two PCB-based EI-core structure integrated transformers are applied to a 6.6 kW full-bridge single-phase *CLLC* (1 PCLLC) dc/dc converter with parallel-connected full-bridge rectifiers for a 400 V battery pack of OBC applications [21]. The flux generated by the built-in leakage flux will flow inside the magnetic path, and its maximum flux density will be determined by the summation of magnetizing flux and leakage flux. As in higher voltage applications, the voltage second across the transformer becomes larger, resulting in a larger core volume or more turn number of transformers. A series connection of multiple EI-core structure integrated transformers can help reduce each transformer's voltage second and power loss. And with higher power applications, the leakage flux becomes more significant due to the larger current. The matrix transformer concept can be beneficial in reducing magnetic loss and improving the power density of the magnetics [27], [28], [29], [34], [36], [37]. The two EI-core structure integrated transformers can be further integrated into one component to achieve evenly distributed flux, reduced core loss, and lower volume by removing the center legs [37]. The concept can be extended to a scalable matrix integrated transformer based on multiple EI-core structures integrated transformers in [20] with reduced core loss and improved power density. The proposed matrix transformer based on three EI-core structure integrated transformers was implemented on an 11 kW 1 PCLLC with a full-bridge rectifier that achieved 98.4% peak efficiency and 250 W/in^3 power density, and the concept can be extended to multiple EI-core structure integrated transformers. Three-phase converters are more suitable for higher power applications due to automatic current sharing among three phases and lower root-mean-square (RMS) current stress compared with single-phase converters [22], [36], [42]. In [22], three EI-core structure integrated transformers were applied to a three-phase CLLC (3 PCLLC) converter with three full-bridge rectifiers, which can integrate three primary resonant inductors, three secondary resonant inductors, and three transformers into one magnetic component to simplify the system. An improved core structure to further reduce the magnetic core loss through achieving evenly distributed flux inside the core plate can be found in [42].

The above-mentioned integrated transformers are designed for each case and lack versatility. In this article, a novel derivation method of integrating magnetizing inductance with leakage inductance was proposed, where it integrates the controllable leakage inductance with magnetizing inductance based on multiple perfectly coupled transformers (PCTs). These multiple PCTs can be further integrated into one component to gain the benefits of much-reduced core loss and increased power density.

The main contributions of this article are summarized as follows.

1) This article proposes a novel derivation method for integrating magnetizing inductance and leakage inductance. The built-in leakage inductance can be adjusted through each PCT winding arrangement and air gap reluctance. Further integration of PCTs into one component can be beneficial with interleaved magnetomotive force (MMF) polarities across transformer legs in reducing the magnetic core loss through better flux distribution inside the core.
2) The proposed method can be extended to a multiple-input multiple-output transformer based on $(m \cdot k)$ PCTs based integrated transformers, which reduce the number of magnetic components and simplify the system's complexity.
3) The proposed method was verified on a 16.5 kW 3 PCLLC converter with a three-phase rectifier for 800 V battery OBC adopting a 3×3 PCTs based integrated transformer with proper optimization. The proposed converter offers an excellent power density of 500 W/in^3 and a peak efficiency of 98.8% that outperforms state-of-the-art designs. A comparison to the state-of-the-art solutions has been presented in Fig. 30 and Table IX of Section V to ascertain the novelty of the proposed work.

The rest of this article is organized as follows. In Section II, the novel integration method based on n pieces of PCTs will be introduced, and the further integration of n PCTs with interleaved MMF polarities across transformer legs will be provided and verified through Maxwell 3-D finite-element analysis (FEA). The calculation of magnetizing inductance and leakage inductance based on the reluctance model will be provided in detail. In Section III, the extension to a multiple-input multiple-output transformer based on the proposed integration method will be provided. A design example of a 3×3 PCTs based integrated transformer for a 3 PCLLC converter will be provided to show its advantages through Maxwell 3-D FEA simulations. Section IV will provide a specific case design based

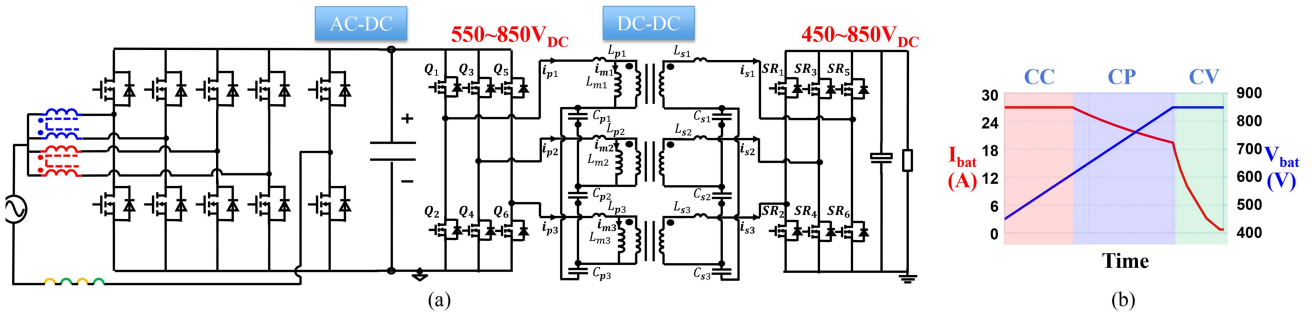

Fig. 4. Topology of two-stage OBC and its charging profile for 800-V battery pack. (a) Main topology. (b) Typical charging profile.

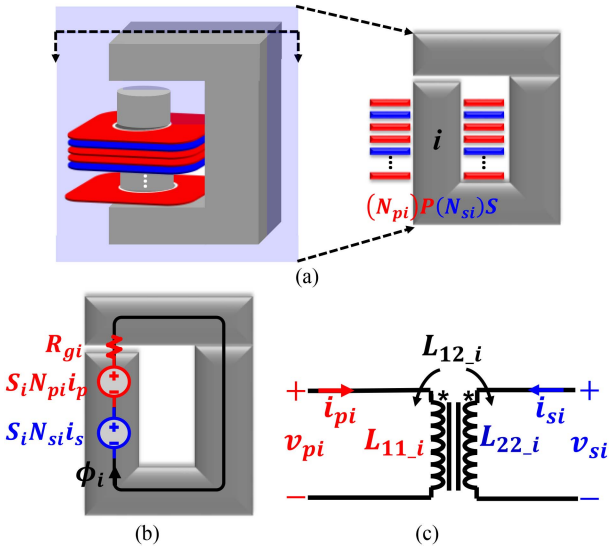

Fig. 5. PCT taking UI core as an example. (a) Transformer structure and section view. (b) Reluctance model. (c) Coupled inductor model.

on the proposed matrix integrated transformer for a 16.5 kW 3 PCLLC converter, consisting of the circuit parameters design, transformer structure, winding arrangement selection, and magnetic loss and footprint optimization. The topology of the 800 V 16.5 kW two-stage bidirectional OBC is shown in Fig. 4(a), and a typical charging profile for an 800 V battery pack is shown in Fig. 4(b). In Section V, the experimental results for the 16.5 kW 3 PCLLC converter with the proposed matrix transformer will be provided to validate the design. Finally, Section VI concludes this article.

II. Universal Method of Magnetizing and Leakage Inductance Integration Based on Multiple PCTs

A. Analysis of PCTs Between Its Primary and Secondary Windings

A PCT has perfect coupling between its primary and secondary windings, then all the fluxes generated by the primary windings will be fully linked with all the secondary windings. The coupling coefficient k is 1. Taking a UI-core-type PCT as an example, Fig. 5 shows its structure and reluctance model with $(N_{pi})P(N_{si})S$ winding arrangements. i means that it is the ith PCT. $(N_{pi})P(N_{si})S$ means that N_{pi} turns of primary windings and N_{si} turns of secondary windings are placed across the core leg with an air gap length of l_{gi}. Two assumptions were made to simplify the magnetic reluctance model: First, the permeability of the core is infinitely large so that the core's reluctance can be assumed to be zero, and second, the leakage flux in the air is very small and can be ignored. Therefore, only the air gap reluctance is considered, which is R_{gi}. S_i is the sign of MMF generated by primary and secondary current in the reluctance model, as shown in Fig. 5(b), which will determine the flux directions φ_i. The value of S_i can be 1 or -1. In the definition of S_i, the direction of generated flux matches with the priority of φ_i, as shown in Fig. 5(b), when $S_i = 1$, and its direction is reversed when $S_i = -1$.

The magnetic flux φ_i can be calculated as follows:

$$\varphi_i\left(i_p, i_s\right) = \left(S_i \cdot N_{pi} i_p + S_i \cdot N_{si} i_s\right)/R_{gi} \tag{1}$$

where the reluctance of air gap can be calculated as follows:

$$R_{gi} = \frac{l_{gi}}{\mu_0 \cdot A_{ei}}. \tag{2}$$

A_{ei} is the cross-sectional area of the core leg, l_{gi} is the air gap length of the core leg, and μ_0 is the permeability of free space.

In general, the terminal equations of the transformer, as shown in Fig. 5(c) can be written as follows:

$$\begin{bmatrix} v_{pi} \\ v_{si} \end{bmatrix} = \begin{bmatrix} L_{11\_i\text{PCT}} & L_{12\_i\text{PCT}} \\ L_{12\_i\text{PCT}} & L_{22\_i\text{PCT}} \end{bmatrix} \frac{d}{dt} \begin{bmatrix} i_{pi} \\ i_{si} \end{bmatrix} \tag{3}$$

where the self-inductances $L_{11\_i\text{PCT}}$ and $L_{22\_i\text{PCT}}$ and mutual inductance $L_{12\_i\text{PCT}}$ can be calculated in (4) based on the reluctance model, as shown in Fig. 5(b)

$$\begin{aligned} L_{11\_i\text{PCT}} &= \varphi_i\left(i_p, 0\right) S_i N_{pi}/i_p = N_{pi}^2/R_{gi} \\ L_{22\_i\text{PCT}} &= \varphi_i\left(0, i_s\right) S_i N_{si}/i_s = N_{si}^2/R_{gi} \\ L_{12\_i\text{PCT}} &= \varphi_i\left(i_p, 0\right) S_i N_{si}/i_p = N_{pi} N_{si}/R_{gi} \\ &= \sqrt{L_{11\_i\text{PCT}} L_{22\_i\text{PCT}}}. \end{aligned} \tag{4}$$

The PCT can be in another format, such as the UI-core-type transformer in [39], which divides the primary and secondary windings into two groups and is placed across the two core legs of the UI core. The core can be replaced by other standardized core types other than UI core to reduce the core loss, where the core shapes can be Toroid, EI, EE, PQ, RM, P-type, etc.

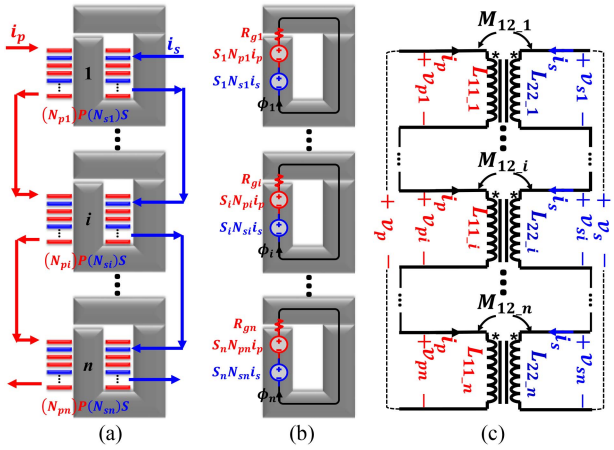

Fig. 6. n discrete PCTs to form an integrated transformer. (a) Transformer structures. (b) Its reluctance model. (c) Electrical circuits.

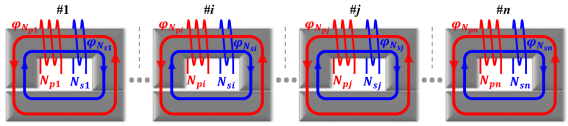

Fig. 7. Flux distribution of n discrete PCTs.

B. Magnetizing Inductance and Leakage Inductance Integration Based on Multiple PCTs

For higher voltage and higher power applications, series connections of PCT can help reduce the voltage second across each elemental transformer and share the total magnetic loss. The PCT in Fig. 5(a) can be adopted as one elemental transformer and n pieces of PCTs can be connected with input-series output-series (ISOS) configuration, as shown in Fig. 6. The flux inside each UI core can be derived in (1), as each PCT is magnetically decoupled. The self-inductances L_{11} and L_{22}, and mutual inductance L_{12} can be calculated in (5) based on the reluctance model, as shown in Fig. 6(b)

$$\begin{aligned} L_{11} &= \sum_{i=1}^{n} \frac{\varphi_i\left(i_p,0\right) S_i N_{pi}}{i_p} = \sum_{i=1}^{n} \frac{N_{pi}^2}{R_{gi}} = \sum_{i=1}^{n} L_{11\_i\mathrm{PCT}} \\ L_{22} &= \sum_{i=1}^{n} \frac{\varphi_i\left(0,i_s\right) S_i N_{si}}{i_s} = \sum_{i=1}^{n} \frac{N_{si}^2}{R_{gi}} = \sum_{i=1}^{n} L_{22\_i\mathrm{PCT}} \\ L_{12} &= \sum_{i=1}^{n} \frac{\varphi_i\left(i_p,0\right) S_i N_{si}}{i_p} = \sum_{i=1}^{n} \frac{N_{pi} N_{si}}{R_{gi}} = \sum_{i=1}^{n} L_{12\_i\mathrm{PCT}}. \end{aligned} \tag{5}$$

Fig. 7 shows the flux distributions of n PCTs. For the ith PCT (i can be 1, 2,…, n), the flux generated by N_{pi} turns of primary windings $\varphi_{N_{pi}}$ is fully linked with N_{si} turns of secondary windings. However, the flux generated by N_{pi} turns of primary windings does not link with N_{sj} ($i \neq j$) turns of secondary windings, which means that the primary windings and secondary windings are not perfectly coupled, and this is the reason for the generation of built-in leakage inductance. The

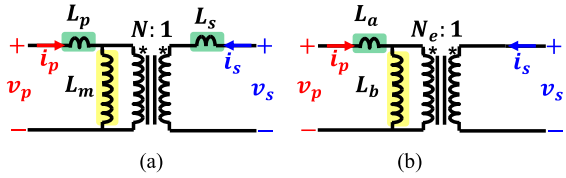

Fig. 8. Transformer models. (a) T-model. (b) Cantilever model.

coupling coefficient $k_{n\mathrm{PCT}}$ can be calculated in (6). The coupling coefficient can be adjusted by assigning different winding arrangements and air gap reluctances for each PCT so that a controllable built-in leakage inductance can be achieved

$$\begin{aligned} k_{n\mathrm{PCT}} &= \frac{L_{12\_n\mathrm{PCT}}}{\sqrt{L_{11\_n\mathrm{PCT}} L_{22\_n\mathrm{PCT}}}} \\ &= \frac{\sum_{i=1}^{n} L_{12\_i\mathrm{PCT}}}{\sqrt{\sum_{i=1}^{n} L_{11\_i\mathrm{PCT}} \sum_{i=1}^{n} L_{22\_i\mathrm{PCT}}}}. \end{aligned} \tag{6}$$

The transformer T model and cantilever model are shown in Fig. 8. The inductance parameters of the T model and cantilever model transformers are listed in (7) and (8). N can be the physical turns ratio between the primary and secondary windings. The inductor parameters for different topologies can be applied to design various converters

$$L_m = NL_{12},\ L_{kp} = L_{11} - NL_{12},\ L_{ks} = L_{22} - L_{12}/N \tag{7}$$

$$L_b = L_{12}^2/L_{22},\ L_a = L_{11} - L_{12}^2/L_{22},\ N_e = \sqrt{L_b/L_{22}}. \tag{8}$$

The inductance ratio between magnetizing inductance and leakage inductance L_n is critical for designing resonant converters. It determines the peak gain of the converter and the operation switching frequency range. With the proper design of N_{pi}, N_{si}, and R_{gi}, and the number of n, different L_n values can be obtained based on (5), (7), and (8).

The approach that splits two PCTs, as presented in [39], is a special case of this concept when $n = 2$ after moving a part of the primary and secondary windings to another core leg and dividing the total air gap into two parts on each core leg. The air gap is equal for the two PCTs.

To explain the idea more straightforwardly, three cases, when $n = 2$, were adopted for Maxwell 2-D FEA analysis using an eddy current solver to evaluate the flux distribution and inductance parameters. The connections of two PCTs are shown in Fig. 9(a). The core leg width is set to 6.2 mm, the model depth is set to 6.3 mm, the primary current excitation i_p is 27.33 A with $-25.2°$ phase angle, and the secondary current excitation i_s is 27.28 A with 0° phase angle. Case 1 has 4*P*2*S* winding arrangement for the first (1st) PCT, 2*P*4*S* winding arrangement for the second (2nd) PCT, and the air gap length of two PCTs is set to 0.7 mm. Compared with case 1, the air gap of 2nd PCT is set to 1.4 mm to analyze its impact on the coupling coefficient. Case 3 has 5*P*3*S* winding arrangement for the 1st PCT, 3*P*5*S* winding arrangement for the 2nd PCT, and the air gap length of two PCTs is set to 1.54 mm. The details of simulated inductance

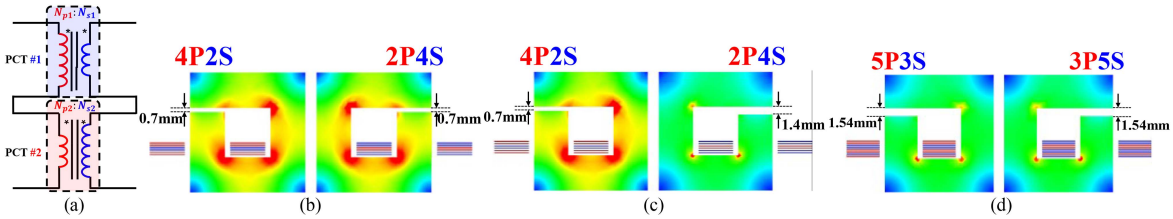

Fig. 9. Connection of 2 PCTs and their 2-D FEA simulation results. (a) Connection circuit. (b) Simulation results of case 1. (c) Simulation results of case 2. (d) Simulation results of case 3.

TABLE I
SIMULATION RESULTS COMPARISON OF DIFFERENT CASES

Parameters	Case 1	Case 2	Case 3
Wind. arrange. of 1st PCT	4*P2S*	4*P2S*	5*P3S*
Wind. arrange. of 2nd PCT	2*P4S*	2*P4S*	3*P5S*
l_{g1} of 1st PCT/mm	0.7	0.7	1.54
l_{g2} of 2nd PCT/mm	0.7	1.4	1.54
L_{11}/μH	12.4	11.40	11.78
L_{22}/μH	12.4	8.40	11.76
L_{12}/μH	9.92	7.92	10.38
Simulated k	0.8	0.810	0.882
Calculated k	0.8	0.816	0.881

and coupling coefficient were provided in Table I, and their flux distribution was compared in Fig. 9(b)–(d).

As the results of case 1 show, the coupling coefficient k is smaller than 1, which means built-in leakage inductance can be achieved with 2 PCTs primary side connected in series and the secondary side in series. In case 2, the air gap length of the second PCT is two times that of the first PCT, which can adjust the coupling coefficient, as Table I shows, and the flux distribution of each PCT will be different, as Fig. 9(c) shows. As Fig. 9(d) shows, the flux density of the PCTs in case 3 can be much smaller by changing the winding arrangement from 4*P2S* and 2*P4S* to 5*P3S* and 3*P5S*, which has a larger coupling coefficient, namely, smaller built-in leakage inductance. The 2-D FEA simulation results prove the effectiveness of integrating built-in leakage inductance with magnetizing inductance based on the proposed method, and the air gap reluctance and winding arrangement can successfully adjust the coupling coefficient. Design tradeoffs should be made when adopting this method when designing the integrated transformer with the proposed method, as different winding arrangements and different air gap lengths will impact the total loss distribution between core loss and winding loss.

C. Integration of Multiple PCTs

Although the built-in leakage inductance can be built with a standardized core shape by assembling n pieces together with the careful design of windings arrangements and air gap reluctance, the core loss increases significantly as the additional flux is generated inside the core, especially with the larger leakage inductance value. It is also challenging to assemble multiple core pieces of PCTs with good tolerance control, and the power density can also be impacted, as more space for fixing the transformers is required.

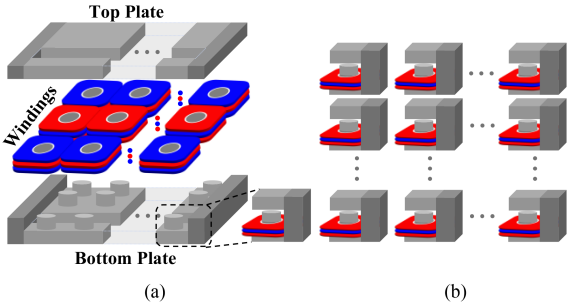

Fig. 10. Example of the proposed n PCTs based integrated transformer. (a) Transformer structure. (b) Equivalent model of n PCTs.

To solve these problems, several PCTs can be integrated into one core, as shown in Fig. 10. The proposed integrated transformer can be built in another format if the other format meets the following requirements.

1) The primary and secondary windings are placed across the core legs, no matter the shape of the core legs.
2) There is at least one additional core leg that has a zero air gap, which means the additional core leg(s) can be treated as zero-reluctance path(s) for the flux generated by the primary and secondary windings to form a PCT, as shown in Fig. 10(a).

When n PCTs are integrated into one core, the same inductance matrix can be found in (5), as all PCTs are magnetically decoupled due to the zero-reluctance path, and its equivalent model can be found in Fig. 10(b), which includes n pieces' PCTs. The benefits of the proposed integrated transformer include better manufacturing capability and smaller core loss with proper design. Based on the proposed n PCTs based integrated transformer, different turns' ratios, other than 1:1, can be achieved, and the air gap reluctance across each transformer leg provides a new control variable to adjust the built-in leakage inductance in a smooth step. This proposed transformer can be scaled up by adding more PCTs, and it can be extended to multiple-input multiple-output transformer applications, which will be discussed in Section III.

D. Interleaved MMF Polarity Across Transformer Core Legs to Reduce Core Loss

For each PCT, as shown in Fig. 10(b), the generated flux can only flow in one direction and will be determined by the priority of the MMF caused by the primary and secondary current across the core legs, namely, the values of S_i, as Fig. 11(a) pointed out.

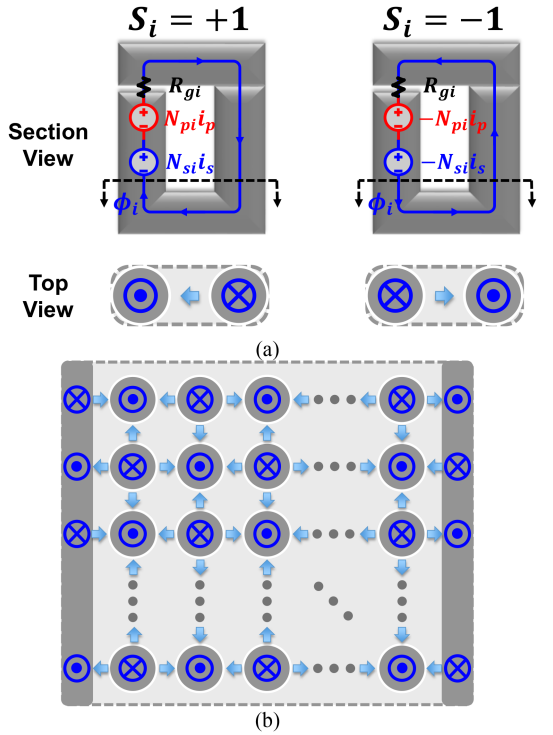

Fig. 11. Flux distribution of interleaved MMF priority structure. (a) Flux direction of PCT with different S_i. (b) Interleaved MMF priorities.

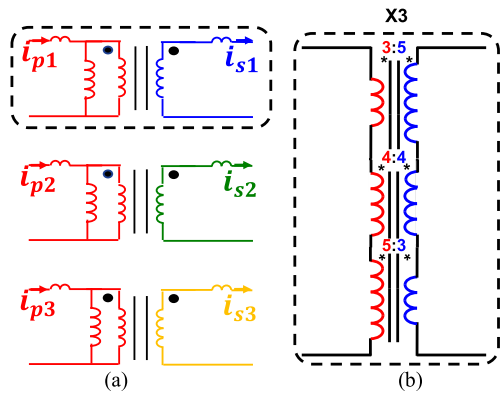

Fig. 12. Electrical circuits of three-phase transformers. (a) Circuits of three phases. (b) Circuits inside each phase.

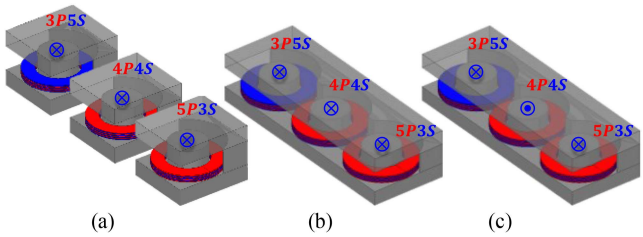

Fig. 13. Different simulation models. (a) Model 1: discrete 3 PCTs. (b) Model 2: 3 PCTs based integrated transformer with the same MMF polarity. (c) Model 3: 3 PCTs based integrated transformer with interleaved MMF polarities.

The selection of S_i will not impact the values of inductance. However, it will impact the flux distribution and core loss. An interleaved MMF polarities across core legs are preferred for the matrix n PCTs based integrated transformer, as Fig. 11(b) shows, which means that the values of S_i for the two adjacent core legs are reversed. This interleaved MMF priority structure will make the flux more evenly distributed in the core plate, resulting in a much smaller core loss than n pieces of separate PCTs, as a smaller flux density is achieved.

E. Comparison Based on Maxwell FEA Simulation

To better explain the concept of interleaved MMF polarities, a 3 PCLLC converter, as shown in Fig. 4(a), with the three proposed n PCTs based integrated transformers, as shown in Fig. 10, is considered. Fig. 12(a) shows the circuits of three-phase transformers, and Fig. 12(b) shows the detailed circuits of each phase with 3 PCTs.

Several simulation models were built in Ansys Maxwell using 3-D eddy current solver, which include Model 1, 3 discrete PCTs for the transformer and inductors of one phase, as shown in Fig. 13(a); Model 2, 3 PCTs based integrated transformer for the transformer and inductors of one phase with the same MMF polarity, as shown in Fig. 13(b); and Model 3, 3 PCTs based integrated transformer of one phase with interleaved MMF polarities, as shown in Fig. 13(c). As shown in Fig. 13, the transformer and inductor for each phase were formed based on three PCTs with 3*P*5*S*, 4*P*4*S*, and 5*P*3*S* winding arrangements separately. The winding arrangements for each PCT across different models are consistent, ensuring the same MMF distribution and similar winding loss. This consistency in winding loss makes the effects on core loss after integration more evident. The detailed settings for simulation are as follows The core material is DMR96A from Hengdian Dongci Magnetic Group Corporation (DMEGC). For each PCT, a 184 mm^2 cross-sectional area, 6.2 mm winding width, and 0.5 mm air gap length are selected; core plate thickness $h_c = 6$ mm, length of core legs $l_c = 8$ mm, length of side leg $l_{c2} = 8.5$ mm, primary current excitation i_p is 27.083 A with $-24.22°$ phase angle, secondary current excitation i_s is 26.556 A with 0° phase angle. The current excitations are based on a 3 PCLLC converter, as shown in Fig. 4(a), under $V_{\text{in}} = 700$ V, $V_o = 700$ V, $P_o = 16.5$ kW, $f_r = 250$ kHz, $L_m = 28$ μH, and $L_{rp} = L_{rs} = 2.45$ μH. Details on obtaining the amplitude and phase information for current excitation are provided in Appendix A.

The maximum flux density distribution in one switching period based on Maxwell 3-D FEA simulation is provided to evaluate the flux distribution inside the core and explore the benefits of integration with interleaved MMF polarities. Fig. 14(a) shows the flux distribution of three separate PCTs, and the generated flux in each core can only flow from the center leg to the side leg through the core plate. In model 2 with the same MMF polarity, the generated flux can share the same magnetic path in core plates and sides and achieve a better flux distribution inside the core, as shown in Fig. 14(b). A more evenly distributed flux can be achieved with interleaved MMF polarities, as shown in Fig. 14(c). The simulation results comparison for different

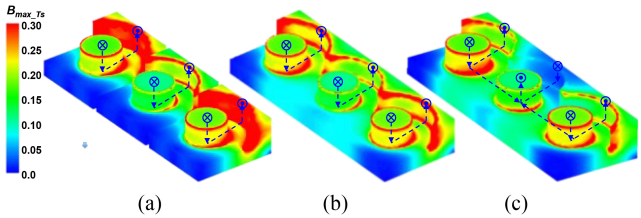

Fig. 14. Simulation results of different simulation models. (a) Model 1: discrete 3 PCTs. (b) Model 2: 3 PCTs based integrated transformer with the same MMF polarity. (c) Model 3: 3 PCTs based integrated transformer with interleaved MMF polarities.

TABLE II
COMPARISON OF DIFFERENT SIMULATION MODELS

Parameters	Model 1	Model 2	Model 3
L_m/μH	28.0	28.0	28.1
$L_{rp}/L_{rs}/\mu$H	2.46	2.49	2.45
Core Loss/W	37.7	29.1	20.4
*Winding Loss/W	20.98	20.86	20.85
Normalized Core Loss	100%	77.2%	54.1%
*Winding Loss is evaluated based on 3-D FEA Simulation			

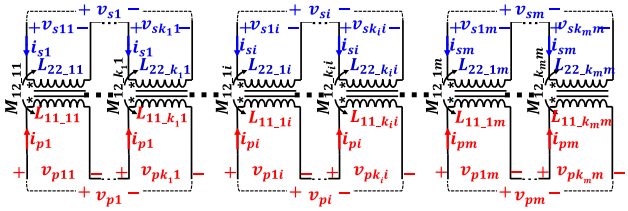

Fig. 15. Electrical circuits of m-input m-output transformer.

models can be found in Table II, which shows that all models can integrate the same leakage inductance with magnetizing inductance, and the 3 PCTs based integrated transformer with interleaved MMF polarities of model 3 can achieve 45.9% core loss reduction.

The above analysis and simulation results show the success of integrating leakage inductance into magnetizing inductance based on multiple PCTs, where each PCT can use a standardized core to build. However, the integrated leakage flux will cause additional core loss, so an n PCTs based integrated transformer with interleaved MMF polarities across transformer legs can be adopted for better flux distribution and core loss reduction.

III. EXTENSION TO MULTIPLE-INPUT MULTIPLE-OUTPUT TRANSFORMER

A. Extension to Multiple-Input Multiple-Output Transformer

An m-inputs, m-outputs transformer can be achieved based on $(\sum_{i=1}^{m} k_i)$ PCTs based integrated transformer as the circuits, as shown in Fig. 15, which can be used for multiphase dc/dc converters, such as the three-phase *LLC/CLLC* resonant converters. For each input and output, k_i PCTs are connected in ISOS connections to form a k_i PCTs based integrated transformer. There are m k_i PCTs based integrated transformers to form a multiple-input multiple-output transformer, as shown in Fig. 16.

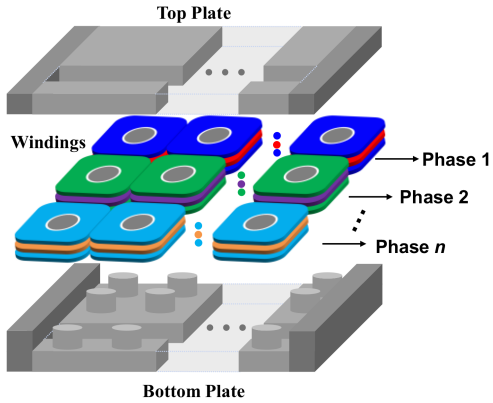

Fig. 16. Transformer structure of an m-input m-output transformer.

Due to the existence of a zero-reluctance path, there will be no coupling among the transformers of each phase. However, the flux density distribution will differ after integrating all phases into one component, which will be discussed in Section III-B.

The inductance matrix for the m-inputs and m-outputs transformer is derived in (9) shown at the bottom of the next page and (10) where

$$L_{pipi} = \sum_{j=1}^{k_i} \left(N_{pij}^2/R_{gij}\right), L_{sisi} = \sum_{j=1}^{k_i} \left(N_{sij}^2/R_{gij}\right)$$

$$L_{pisi} = \sum_{j=1}^{k_i} \left(N_{pij}N_{sij}/R_{gij}\right),$$

$$L_{pipl} = 0\,(i \neq l)\,, L_{sisl} = 0\,(i \neq l)$$

$$L_{pisl} = 0\,(i \neq l)\,,$$

$$L_{sipl} = 0\,(i \neq l)\,. \tag{10}$$

The $(\sum_{i=1}^{m} k_i)$ PCTs based integrated transformer for m-inputs and m-outputs' applications can use discrete PCTs based on standardized core shapes, several partially integrated cores, or one integrated core, as shown in Fig. 16, to reduce the number for magnetics and explore the benefits of core loss reduction after integration.

B. Example of 3 × 3 PCTs Based Integrated Transformer for 3 PCLLC Converter

To better explain this concept, a 3 PCLLC converter, as shown in Fig. 4(a), with the proposed three-input three-output integrated transformer, as shown in Fig. 16, is considered. Based on the 3 PCTs based integrated transformer, as proposed in Fig. 13(c), a new model 4 in Maxwell can be built by integrating three of them into one component, as shown in Fig. 17. The amplitude of current excitation for three phases is set identically, as described in Section II-E, and their phase delay is set to 120° phase delay among phases.

Fig. 18(a) shows the flux distribution of three 3 PCTs based integrated transformers, and Fig. 18(b) shows the flux distribution of 3 × 3 PCTs based three-phase integrated transformers under $V_{\text{in}} = 700$ V, $V_o = 700$ V, $P_o = 16.5$ kW, $f_r = 250$ kHz,

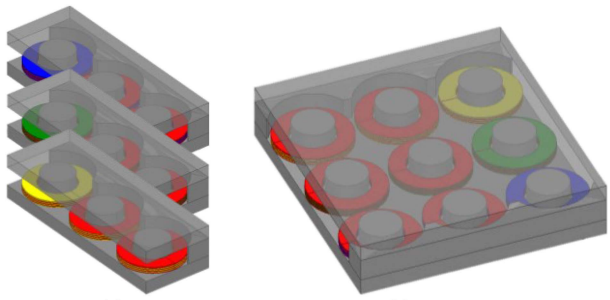

(a) (b)

Fig. 17. Simulation models for three-phase integrated transformer. (a) Three pieces of model 3. (b) Model 4: Integration of three model 3 into one component.

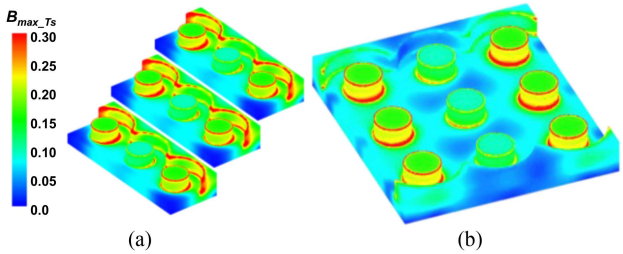

(a) (b)

Fig. 18. Simulation results of different simulation models. (a) Three pieces of model 3. (b) Model 4: integration of three model 3 into one component.

TABLE III
COMPARISON OF DIFFERENT SIMULATION MODELS

Parameters	Model 3 × 3	Model 4	Model 5
L_{m1}– L_{m3}/μH	28.1	28.0	28.0
L_{rp1}– L_{rp3}/L_{rs1}– L_{rs3}/μH	2.45	2.45	2.44
Core Loss/W	61.2	46.9	57.9
*Winding Loss/W	62.54	62.52	62.74
Normalized Core Loss	100%	76.6%	94.6%
Footprint/mm^2	9000	9000	8500
*Winding Loss is evaluated based on 3-D FEA Simulation			

$L_m = 28\ \mu$H, and $L_{rp} = L_{rs} = 2.45\ \mu$H. After integrating three 3 PCT-based integrated transformers with interleaved MMF polarities into one 3 × 3 PCTs based integrated transformer, the flux can be more evenly distributed, as shown in Fig. 18. Furthermore, the core loss can be further reduced. The simulation results comparison for different models of three-phase integrated transformers can be found in Table III. The 23.4% core loss can be achieved with 3 × 3 PCTs based integrated transformer rather than three separate 3 PCTs based integrated transformers. Compared with the solutions of discrete 3 PCTs

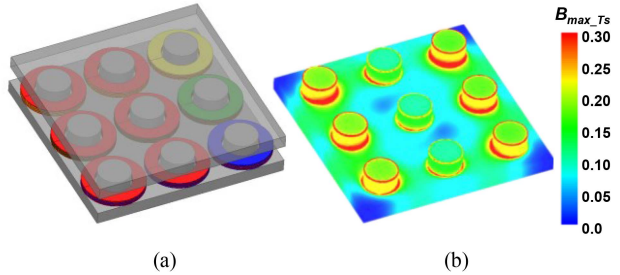

(a) (b)

Fig. 19. Simulation model 5 and its FEA simulation results. (a) Model 5: removing sides legs based on model 4. (b) Its 3-D FEA simulation results.

for each phase, the total magnetic loss can be reduced from 113.1 to 46.9 W, which results in a 58.5% reduction. As Li et al. [22] pointed out, the summation of the generated flux goes through the side legs equal to zero due to the current excitation of three phases having the same amplitude and 120° phase delay among phases. Therefore, these side legs can be removed and built-in model 5, as shown in Fig. 19(a). The flux density distribution inside the core plates can be shown in Fig. 19(b). As Table III presents, it has higher core loss than 3 × 3 PCTs based integrated transformer after removing the sides, while it is still competitive over three separate 3 PCTs based integrated transformers in terms of core loss and footprint.

The increased core loss in model 5 compared with model 4 is due to a higher flux density inside the core plates, as evident from comparing Fig. 18(b) with Fig. 19(b). In model 4, some flux is diverted to the side legs, resulting in a lower flux density in the core plates than in model 5, where there are more green areas indicating a larger flux density.

Model 5 is a specific example of model 4 by removing the side legs; this is only valid for a three-phase integrated transformer. Although the removal of side legs increases the core loss, its structure has the potential to be applied for future applications due to some advantages: First, the copper winding can be easily accessed after removing the side legs, which is good for thermal management; Second, the length of side legs and core legs do not need to be controlled precisely when a small gap is used (The gap will be determined by the side gap length minus the main core legs' length), which can help save the cost of ferrite cores.

In this article, model 4 was chosen for the design of three-phase integrated transformers because it exhibits the lowest magnetic loss.

For implementing the proposed integrated transformer in other multiphase applications, it is crucial to assess the design

$$\begin{bmatrix} v_{p1} \\ v_{s1} \\ v_{p2} \\ v_{s2} \\ \vdots \\ v_{pm} \\ v_{sm} \end{bmatrix} = \begin{bmatrix} L_{p1p1} & L_{p1s1} & 0 & 0 & \dots & 0 & 0 \\ L_{p1s1} & L_{s1s1} & 0 & 0 & \dots & 0 & 0 \\ 0 & 0 & L_{p2p2} & L_{p2s2} & \dots & 0 & 0 \\ 0 & 0 & L_{p2s2} & L_{s2s2} & \dots & 0 & 0 \\ \vdots & \vdots & \vdots & \vdots & \ddots & \vdots & \vdots \\ 0 & 0 & 0 & 0 & \dots & L_{pmpm} & L_{pmsm} \\ 0 & 0 & 0 & 0 & \dots & L_{pmsm} & L_{smsm} \end{bmatrix} \frac{d}{dt} \begin{bmatrix} i_{p1} \\ i_{s1} \\ i_{p2} \\ i_{s2} \\ \vdots \\ i_{pm} \\ i_{sm} \end{bmatrix} \tag{9}$$

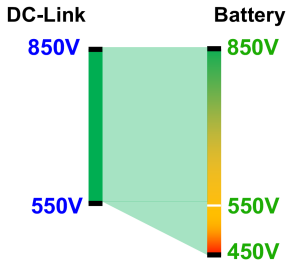

Fig. 20. Mapping between DC-link voltage and battery voltage.

TABLE IV
SPECIFICATION OF 16.5-KW 3 PCLLC CONVERTER

Parameters	Values
Input voltage range, V_{in}	550–850 V
Output voltage range, V_o	450–850 V
Maximum output power, P_{o_max}	16.5 *k*W
Maximum output current, $I_{o\ max}$	27 A

of the low-reluctance path. This includes selecting appropriate cross-sectional areas and their physical placements. Using a 3-D FEA simulation tool is essential to examine the flux distribution and prevent flux accumulation in the low-reluctance path(s).

IV. DESIGN OF PROPOSED THREE-PHASE INTEGRATED TRANSFORMERS FOR A 16.5 KW 3 PCLLC CONVERTER

A. Circuits Parameter Design

To validate the proposed 3 × 3 PCTs based three-phase integrated transformer, a 3 PCLLC converter for a 16.5-kW bidirectional OBC was designed and implemented. The topology of the two-stage bidirectional OBC is shown in Fig. 4(a). As the authors in [6], [9], and [20] point out, the flexible dc-link voltage concept allows the 3 PCLLC converter running at the resonant frequency to achieve the best efficiency for dc/dc stage, and its overall efficiency of the two-stage structure is still higher than the fixed dc-link voltage solution. The flexible dc-link voltage was adopted in the design of the 3 PCLLC converter. The output voltage range for this OBC is from 450 to 850 V, and the dc-link voltage range is from 550 to 850 V. The mapping between the dc-link voltage and battery voltage is shown in Fig. 20. For the battery voltage from 450 to 550 V, the 3 PCLLC converter operates higher than the resonant frequency to satisfy the voltage gain lower than one and regulate the double-line-frequency ripple. For battery voltage higher than 550 V, it operates around the resonant frequency to regulate the double-line-frequency ripple in the dc-link voltage and achieve the highest efficiency.

In the design of dc/dc stage, the input and output specifications are shown in Table IV. As shown in Fig. 20, the input and output voltage ranges are very close so that the turns ratio of the transformers is chosen to 1. The resonant frequency is set to 250 kHz, and the core material is DMR96A from DMEGC. The magnetizing inductance is 28 μH, and the required primary/secondary leakage inductance is 2.44 μH; the ratio between magnetizing inductance and leakage inductance is 11.5 so that ZVS of all power devices can be achieved, and the gain characteristics can meet the regulation requirements. The similar circuit design steps of a bidirectional *CLLC* converter for OBC application can be found in [20], including the design of magnetizing inductance, resonant inductance, and the selection of power devices.

TABLE V
DESIGN PARAMETERS OF RESONANT COMPONENTS

Parameters	Values
Resonant frequency, f_r	250 kHz
Magnetizing inductance, L_m	28 μH
Primary/secondary resonant inductance, L_r	2.44 μH
Inductance ratio, L_m/L_r, L_n	11.5
Primary/secondary resonant capacitors, C_r	56.0 nF

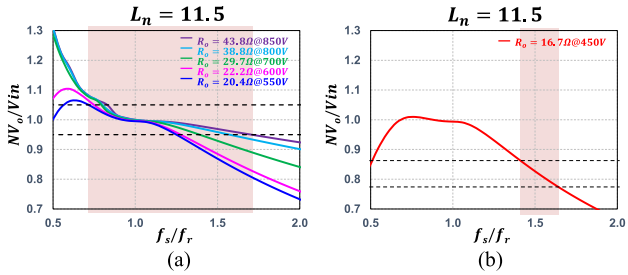

Fig. 21. Gain characteristics of different conditions at L_n=11.5. (a) Region 1: V_o is from 550 to 850 V. (b) Region 2: V_o is 450 V.

The design parameters of the 16.5 kW 3 PCLLC converter are listed in Table V. The voltage gain characteristics at different load conditions based on the design parameters are shown in Fig. 21. Considering a 10% ripple on dc-link voltage, the voltage gain range at $L_n = 11.5$ is proved to achieve the required voltage gain range within a considerable frequency range.

B. Transformer Structure and Winding Arrangements

Based on the L_n selected in Section IV-A, the integrated transformer's winding arrangements of each phase for the proposed 3 × 3 PCTs based three-phase integrated transformer can be shown in Fig. 13(c), which are 5*P*3*S*, 4*P*4*S*, and 3*P*5*S* for each PCT with the same air gap length. The inductance matrix of the couple inductor model can be calculated in (11) based on (5). The magnetizing inductance L_m, primary leakage inductance L_{kp}, secondary leakage inductance L_{ks}, and inductance ratio among L_m, L_{kp}, and L_n, can be calculated in (12) based on (7) and (11)

$$L_{11} = \sum_{i=1}^{n} \frac{N_{pi}^2}{R_{gi}} = \frac{50}{R_g}, \quad L_{22} = \sum_{i=1}^{n} \frac{N_{si}^2}{R_{gi}} = \frac{50}{R_g}$$
$$L_{12} = \sum_{i=1}^{n} \frac{N_{pi}N_{si}}{R_{gi}} = \frac{46}{R_g} \tag{11}$$

$$L_m = \frac{46}{R_g}, \quad L_{kp} = L_{ks} = \frac{4}{R_g}, \quad L_n = \frac{L_m}{L_{kp}} = 11.5. \tag{12}$$

The air gap reluctance can be adjusted to achieve the required magnetizing inductance and leakage inductance by designing the cross-sectional area and air gap length.

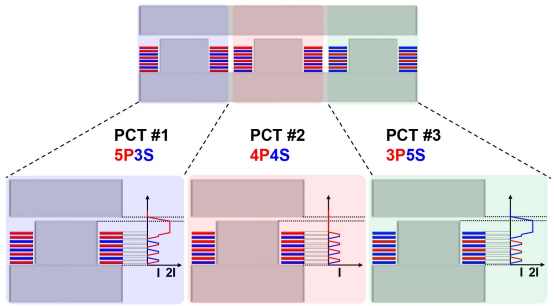

Fig. 22. MMF distribution across each transformer leg for each PCT.

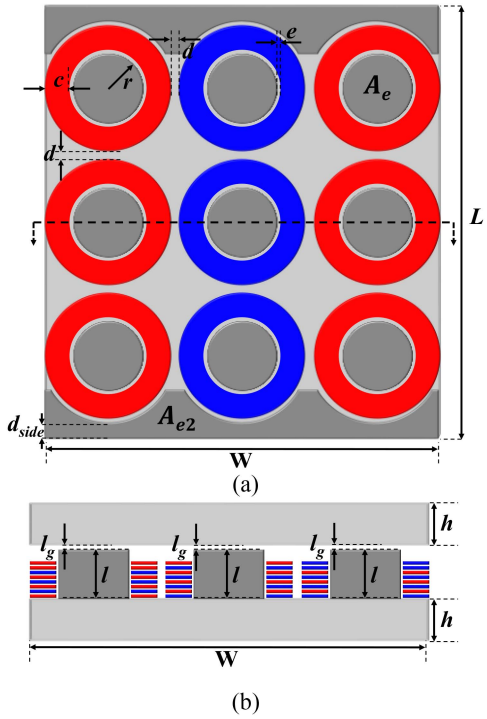

Fig. 23. Transformer dimensions. (a) Top view. (b) Section view.

Interleaving winding arrangements are preferred, as it can achieve smaller MMF across the transformer legs and smaller ac winding loss, as shown in Fig. 22.

Fig. 23 shows the front and sectional views of the transformer structures and winding arrangements, where r is the radius of the core leg, c is the winding width, h is the thickness of the core plate, L is the length of the transformer, and W is the width of the transformer. The length of the core leg is set to the thickness of PCB board plus five times the air gap to avoid any fringing effect from the flux. The cross-sectional area of the core plate A_e is set to three times the cross-sectional area of the core leg. The cross-sectional area of the side legs can be defined as A_{e2} and equals A_e so that d_{side} can be calculated. The distance between windings d is set to 2 mm. The distance between the winding and the core e is set at 1 mm to ensure that the core leg can fit the holes in the PCB.

The footprint FT is a rectangle covering all windings and cores. The values of L, W, h, and FT can be calculated in (13)–(16)

$$L = 6c + 6r + 2d + 8e + 2d_{\text{side}} \tag{13}$$

$$W = 6c + 6r + 2d + 6e \tag{14}$$

$$h = 3\pi r^2 / W \tag{15}$$

$$\text{FT} = L \cdot W. \tag{16}$$

By sweeping, r and c, winding loss, core loss, and total transformer loss at different footprints can be determined.

TABLE VI
MEASURED PARAMETERS OF DMR96A AT 250 KHZ

Parameters	Values
Relative Permeability	3500
Relative Permittivity	80 653
Bulk Conductivity	0.484 S/m
Dielectric Loss Tangent	0.38

C. Magnetic Loss and Footprint Optimization

Instead of Dowell's 1-D model [43], [44], a 2-D Maxwell FEA simulation was implemented to evaluate the winding loss by considering the impact of the fringing effect of the air gap to achieve certain magnetizing inductance [21].

In a planar matrix transformer with multiple core legs, the generated flux will not flow in one direction, and its distribution is highly dependent on the winding arrangement. The adoption of the Steinmetz equation cannot predict the core loss accurately. Furthermore, the core dimension, nonuniform flux distribution, dimension resonance, eddy current loss, and skin effect analyzed in [45] significantly impact the core loss characterization. Therefore, Maxwell 3-D FEA simulation, which considers these factors, was adopted for evaluating the core loss.

DMR96A from DMEGC was selected due to its competitive low core loss density at the 250 kHz switching frequency over other candidates [20]. The critical magnetic parameters for Maxwell simulation are tested based on the method adopted in [45] and shown in Table VI. The copper thickness in each layer is selected to be 4 Oz according to the skin depth of copper at 250 kHz, and the excitation is based on 700-V battery voltage and 16.5-kW output power.

Based on the above-mentioned information, the 2-D FEA and 3-D FEA simulation models of the proposed three-phase integrated transformer were built in ANSYS Maxwell with the same winding arrangements and current excitations, as shown in Fig. 22. The core leg radius r was swept in a range from 6 to 14 mm, and winding width c was swept in a range of 3–12 mm, the core loss, winding loss, and its total magnetic loss can be evaluated, and the 3-D surface plot of total loss at different r and c and its 2-D contours can be shown in Fig. 24(a) and (b). As the 3-D surface of total magnetic loss shows, the desired design point should be larger radius to reduce the core loss and larger winding width to reduce the winding loss, aligning with the trajectory of the solid pink line to achieve a small total loss. However, reducing magnetic loss is a tradeoff between total magnetic loss and the footprint, which is a function of r and c. Therefore,

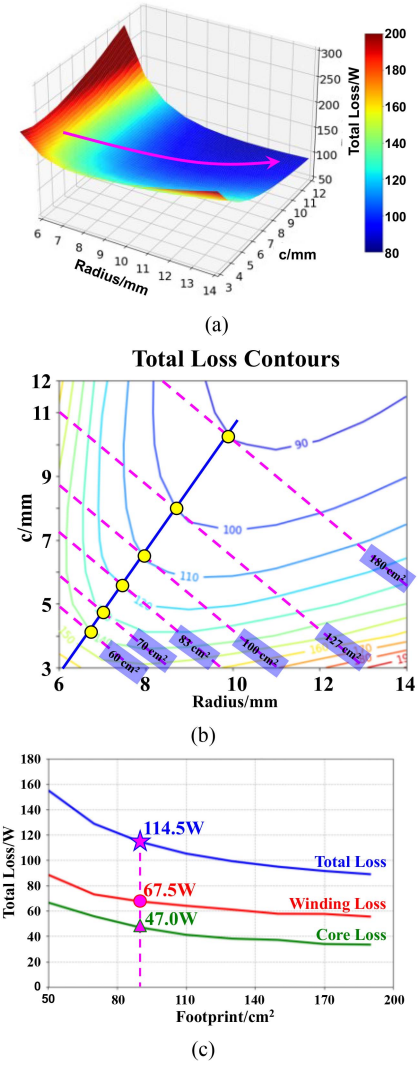

Fig. 24. Total magnetic loss. (a) Three-dimensional surface plot. (b) Two-dimensional contour. (c) Minimum magnetic loss at different footprints.

the contours of total loss within the design region are shown in Fig. 24(b), where the total magnetic losses on each solid line are the same. In Fig. 24(b), there are dashed pink lines representing different footprints, and the tangent points between the dashed lines and total loss contours are the minimum loss design points at a specifically given footprint. Furthermore, the magnetic loss optimization can be performed to achieve the tradeoff between transformer winding loss and core loss at different footprints based on the minimum magnetic loss at different footprints, as shown in Fig. 24(c). The choice of the design's footprint size was made with careful consideration of the layout requirements for a high-power-density power converter, resulting in a selected area of 90 cm^2. Table VII displays the comprehensive set of design parameters in detail. The loss breakdown of the converter at $V_{\rm in} = 700$ V and $P_o = 16.5$ kW can be shown in Fig. 25.

At given magnetizing inductance L_m, built-in leakage inductance L_{kp}/L_{kp}, and turns ratio N_p/N_s, several important design considerations need to be considered.

1) For manufacturing consideration, the cross-sectional area of each PCT can be designed to the same values, and the air gap in each core leg is set to the same value for first consideration. This structure is easier for manufacturing and lower cost in controlling the air gaps. The cross-sectional area or air gap can be adjusted in a small step to adjust the built-in leakage inductance to a desired value.
2) The number selection of PCTs and their winding arrangements are highly dependent on the designed turns number, inductance parameters (L_m and L_{kp}/L_{ks}), and cost. The PCB layers can be selected based on cost considerations and required inductance ratio between L_m and L_{kp}/L_{ks}. In this design, eight layers and one winding per layer were adopted. The design process can start with a pure transformer by distributing the turns number of primary windings and secondary windings into each PCT evenly, and then change the turns number of each PCT different from that of a pure transformer to integrate the required built-in leakage inductance. More PCTs can be added if the required built-in leakage inductance cannot meet the requirement.
3) The turns number of PCTs should be designed as closely as possible to ensure a similar flux amplitude for all PCTs, namely, evenly core loss density.
4) For winding loss consideration, the primary windings and secondary windings of each PCT should be placed interleaved to reduce the winding loss by reducing the MMF accumulation.
5) After selecting the turns number of all PCTs, a similar design procedure, as presented in Section IV-C, should be implemented to achieve the optimized case at a given design point.

However, as the turns number of primary windings and secondary windings are integers, the magnetizing inductance and

TABLE VII
DESIGN PARAMETERS OF THE PROPOSED INTEGRATED TRANSFORMER

Design Parameters	Values
Core material	DMR96A
Copper thickness of PCB	4oz
Radius of the core leg, r	7.65 mm
Winding width, c	6.0 mm
Length of core, L	98.0 mm
Width of core, W	91.9 mm
Length of core legs, l	8.0 mm
Length of core plate, h	6.0 mm
Length of air gap, l_g	0.5 mm
Length of d_{side}	2.0 mm
Footprint, FT	9000 mm^2

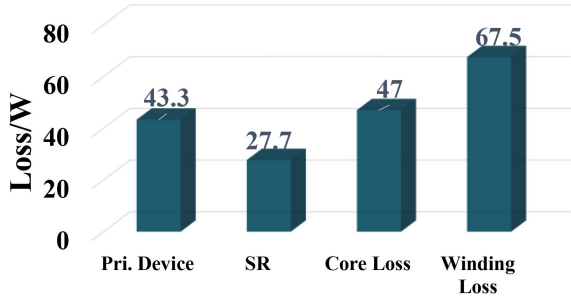

Fig. 25. Loss breakdown at $V_{\rm in} = 700$ V and $P_o = 16.5$ kW.

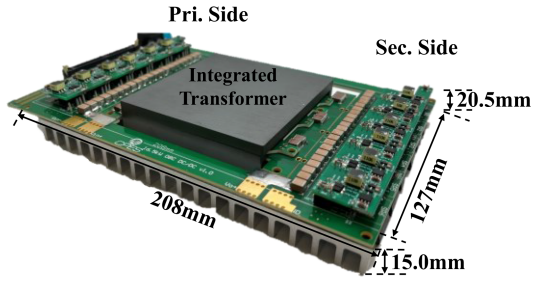

Fig. 26. Prototype picture.

TABLE VIII
DESIGN PARAMETERS OF 16.5 KW DC/DC PROTOTYPE

Design Parameters	Values
Input Voltage, V_{in}	550V–850V
Output Voltage, V_o	450V–850V
Maximum Output Power, P_{omax}	16.5 kW
Maximum Output Current, I_{omax}	27 A
Primary and Secondary SiC Devices	C3M0021120K
Gate Driver of SiC Devices	UCC21750
Core Material	DMR96A
Resonant Frequency, f_r	250 kHz
Magnetizing Inductance, L_m	27.8 μH
Resonant Inductance, L_{p1}–L_{p3}/L_{s1}–L_{s3}	2.45 μH
Resonant Capacitors, C_{p1}–C_{p3}/C_{s1}–C_{s3}	56.0 nF
PCB	4 Layers + 4 Layers, 4 oz. Cu., 1.6 mm thick.
Prototype Dimension w/o Heat Sink	208*127*20.5 mm
Dimension of Heat Sink	208*127*15 mm

built-in leakage inductance can be adjusted through discrete steps. It is important to thoughtfully design the number of turns for all PCTs to achieve the desired parameters.

V. EXPERIMENTAL RESULTS

In this article, an SiC-based 250 kHz 16.5 kW 3 PCLLC converter, which serves as the second stage of an OBC, was built with a proposed 3 × 3 PCTs based three-phase integrated transformer, as depicted in Fig. 26. To optimize cost-effectiveness, the design utilizes two separate four-layer PCBs: a primary motherboard and a secondary daughter board. The motherboard accommodates all essential components, including four turns of windings, resistors, capacitors, and various devices. In parallel, the daughter board contains an additional four turns of windings. Copper connectors were soldered to establish the necessary electrical connections between the boards. Both boards share the same layer stack-up with a thickness of 1.6 mm. The critical design parameters and components employed for the 16.5-kW 3 PCLLC dc/dc converter are summarized in Table VIII. Notably, the power density achieved by the power stage reaches 500 W/in^3.

The input voltage and output voltage specifications are detailed in Table VIII. To optimize the performance of the dc/dc stage across most battery voltage ranges (550–850 V), the variable dc-link concept is applied [6], [20], ensuring that the converter operates around the resonant frequency. In instances where the battery voltage falls within the range of 450–550 V, variable frequency control is employed to reduce the voltage gain.

Fig. 27 illustrates the operation waveform of a 3 PCLLC resonant converter utilizing the proposed 3 × 3 PCTs based three-phase integrated transformer, specifically in the charging mode. Due to the inherent symmetrical structure of the 3 PCLLC resonant converter topology with 1:1 turns ratio, the operational principles in the discharging mode closely resemble those in the charging mode. Each figure includes the gate–source waveform of primary switches Q_2 and v_{gs_Q2}, the drain–source waveforms of primary switches Q_2 and v_{ds_Q2}, the gate–source waveform of secondary switches SR_2 and v_{gs_SR2}, the drain–source waveforms of secondary switches SR_2 and v_{ds_SR2}, primary resonant current of three phases i_{p1}, i_{p2}, and i_{p3}, secondary resonant current of three phases i_{s1}, i_{s2}, and i_{s3}, and magnetizing currents i_{m1}, i_{m2}, and i_{m3}. i_{p3} and i_{s3} are calculated based on the KCL of three-phase primary and secondary currents. i_{m1}, i_{m2}, and i_{m3} are calculated from the primary current minus the reflected secondary current to the primary side with a factor of turns ratio. Fig. 27(a)–(d) shows the waveforms at maximum output power for each battery voltage, 450 V/12.15 kW, 550 V/14.85 kW, 700 V/16.5 kW, and 850 V/16.5 kW, respectively. Fig. 27(e) and (f) depicts the waveforms of the 850 V battery voltage under constant voltage charging mode conditions, with output power levels of 8.25 kW and 3.3 kW, respectively. Notably, the waveforms illustrate the achievement of ZVS for both the primary and secondary switches across all conditions. In cases where the battery voltage drops to 450 V, the converter operates at a frequency higher than the resonant frequency to reduce the voltage gain. As indicated by Fig. 27, both the primary and secondary currents exhibit identical amplitudes and maintain a consistent 120° phase shift among all phases, thus confirming the proper operation of the 3 PCLLC converter.

The 250-kHz 16.5-kW 3 PCLLC converter with the proposed 3 × 3 PCTs based integrated transformer can achieve 98.7% peak efficiency over the entire battery voltage range in charging mode. The charging efficiency at full load, with varying battery voltages, is illustrated in Fig. 28(a). In discharging mode, the measured efficiency of the 3 PCLLC converter at different battery voltages is depicted in Fig. 27(b), with a peak efficiency of 98.8%. Fig. 29 presents the thermal performance results of the tested integrated transformer under specific conditions: 700 V input voltage, 16.5 kW output power, and 800 linear feet/min air cooling at a room temperature of 25 °C. The PCB winding's highest recorded temperature is 81.3 °C, and the core temperature is 66.0 °C.

Table IX provides a comprehensive performance comparison between the proposed converter and various dc/dc converters of other battery chargers, as referenced in [20], [21], [22], [46], [47], [48], [49], [50], [51], [52], [53], [54], and [55]. The proposed converter stands out by delivering competitive maximum charging efficiency while employing fewer switching devices and magnetic components. Fig. 30 illustrates the comparison between the output power of the dc/dc stage and their achievement in power density, demonstrating highly competitive results compared with other solutions. The proposed matrix

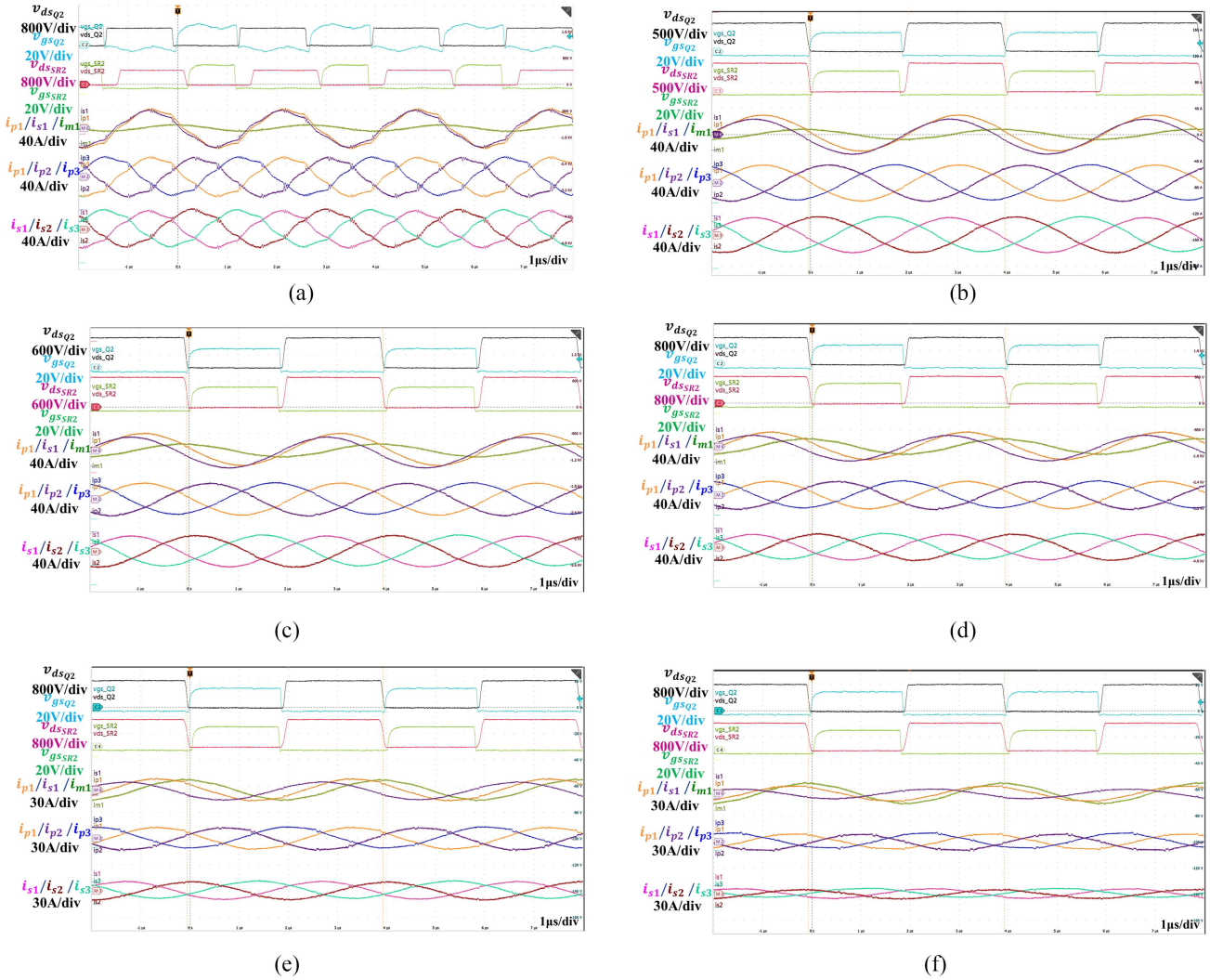

Fig. 27. Key waveforms at different conditions. (a) $V_{\text{in}} = 550$ V, $V_o = 450$ V, and $P_o = 12.15$ kW. (b) $V_{\text{in}} = 550$ V, $V_o = 550$ V, and $P_o = 14.85$ kW. (c) $V_{\text{in}} = 700$ V, $V_o = 700$ V, and $P_o = 16.5$ kW. (d) $V_{\text{in}} = 850$ V, $V_o = 850$ V, and $P_o = 16.5$ kW. (e) $V_{\text{in}} = 850$ V, $V_o = 850$ V, and $P_o = 8.25$ kW. (f) $V_{\text{in}} = 850$ V, $V_o = 850$ V, and $P_o = 3.3$ kW.

TABLE IX
PERFORMANCE COMPARISON OF THIS WORK WITH OTHER SOLUTIONS

Parameter	This work	[20]	[21]	[22]	[46]	[47]	[48]	[49]	[50]	[51]	[52]	[53]	[54]	[55]
Input voltage /V	550–850	550–850	500–840	600–800	800	800	400	380	380~660	800	400	400	380	400
Output voltage /V	450–850	450–850	250–450	300–400	200–950	150–950	250–400	250–380	200–500	150–950	180–430	250–450	–350	100–395
Max. power /kW	16.5	11	6.6	12.5	3.3	6.6	3.2	3.3	6.6	6.6	3.3	10.0	10.5	22
Frequency /kHz	250	250	500	500	65	500	75–300	500	300	500	145–190	100–150	90–275	100
Maximum Efficiency/%	98.8	98.4	97.8	98.2	98.5	98.2	98.5	98.0	98.1	98.4	98.1	96.7	94.5	–97
Full load efficiency/%	95.5–98.7	95.4–98.4	97.3–97.8	96.8–97.9	96–98.5	97–98.2	96.2–98.5	95.9–98.0	96.7–98.0	96.5–98.4	95.6–98.1	93.8–96.7	90.0–95.5	–97
Power density/ kW/L	30.4	15.2	8	9.4	1.4	7.3	4	5.44	~4.9	7.4	0.98	4.6	1.75	3.0
Magnetic Components	1	1	2	1	2	3	2	1	2	2	2	2	6	12
No. of Switch. Devices	12	8	12	12	6	11	8	8	8	11	8	8	18	48

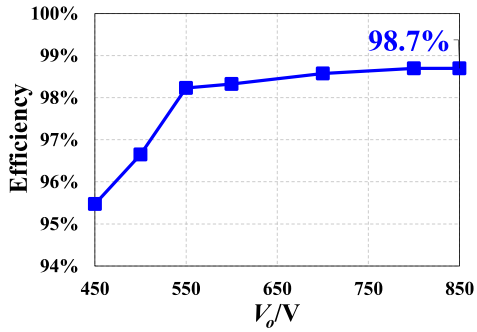

(a)

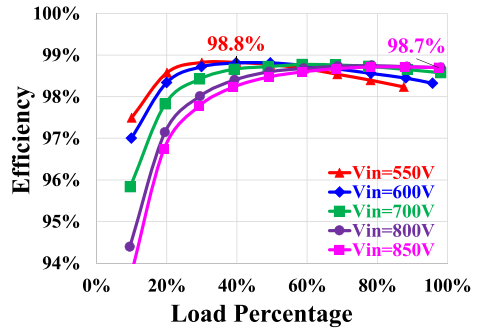

(b)

Fig. 28. Efficiency curves. (a) Efficiency in charging mode. (b) Efficiency of different battery voltages in discharging mode.

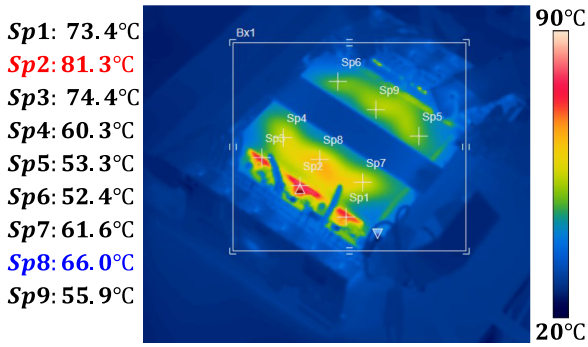

Fig. 29. Thermal performance at $V_{\text{in}} = 700$ V and $P_o = 16.5$ kW.

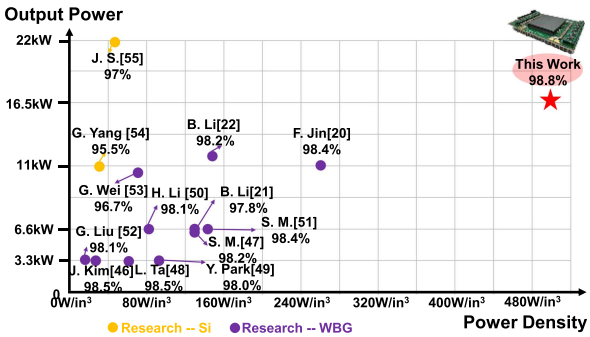

Fig. 30. Power density and output power achievement.

integrated transformer not only enhances a peak efficiency of 98.8% but also enables a higher power density with 500 W/in^3. The 3 PCLLC converter with the proposed matrix integrated transformer emerges as a promising choice for dc/dc stage in 800 V battery charger applications.

VI. Conclusion

The article introduces a generalized approach for integrating leakage inductance into magnetizing inductance using multiple PCTs, thereby substantially simplifying the system. By employing a PCB-based planar integrated transformer as an illustration, it becomes possible to manage the magnetizing and leakage inductance through different PCB winding arrangements and adjust the air gap reluctance of each PCT. Furthermore, incorporating multiple PCTs into a single component substantially reduces core loss, especially when interleaved MMF polarities are implemented across transformer core legs.

The proposed concept has the potential for extension to multiple-input multiple-output integrated transformer applications. This article uses a 3 × 3 PCTs based three-phase integrated transformer as a design example for a 250-kHz 800-V 16.5-kW 3 PCLLC converter. A notable achievement is the significant reduction in core loss observed in the proposed magnetic components compared with the discrete PCTs based integrated transformer. The 16.5-kW prototype achieves a peak efficiency of 98.8% and a power density of 500 W/in^3. The experimental results presented in this article affirm the feasibility and effectiveness of the proposed magnetic integration solution for 800 V OBC applications.

Appendix A

The Maxwell 3-D FEA simulation's eddy current solver was chosen for evaluating the inductance and flux distribution due to its faster simulation speed compared with the transient solver. When operating at the resonant frequency, the primary resonant current i_{p1} and the secondary resonant current i_{s1} are very close to sinusoidal, as shown in Fig. 31. For simplification, only the sinusoidal part was considered. The current excitations of the other two phases are with the same amplitude, but with 120° and 240° phase shift, respectively. The RMS value of primary current and secondary current can be easily calculated and represented by I_{p_rms} and I_{s_rms}, respectively. The representation of primary resonant current $i_{p1(t)}$ and secondary resonant current $i_{s1}(t)$ can be shown in (A1) and (A2), respectively. The phase angle of

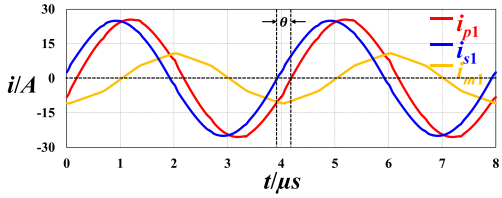

Fig. 31. Simulated current waveforms at $V_{\text{in}} = 700$ V and $P_o = 16.5$ kW.

i_{s1}(t) is set to 0°, and for $i_{p1}(t)$, it is $-\theta°$. θ is determined by the zero-crossing points of i_{p1}(t) and i_{s1}(t), measured in degrees

$$i_{p1}(t) = \sqrt{2} I_{p\_\mathrm{rms}} \sin\left(2\pi f_s \cdot t - \frac{\theta}{180}\pi\right) \tag{A1}$$

$$i_{s1}(t) = \sqrt{2} I_{s\_\mathrm{rms}} \sin\left(2\pi f_s \cdot t\right). \tag{A2}$$

In the eddy current solver, the primary and secondary windings of phase 1 can be set with the amplitude and phase of $i_{p1}(t)$ and $i_{s1}(t)$. The other two phases can have the same amplitude but with additional phase shifts of 120° and 240°.

ACKNOWLEDGMENT

The authors would like to thank Prof. F. C. Lee of Virginia Tech for his valuable and constructive suggestions during the planning and development of this research work. His willingness to give his time so generously has been very much appreciated. This work was conducted with the use of core samples donated in kind by DMEGC.

REFERENCES

[1] 2022. [Online]. Available: https://www.europarl.europa.eu/news/en/headlines/economy/20221019S TO44572/eu-ban-on-sale-of-new-petrol-and-diesel-cars-from-2035 explained

[2] 2023. [Online]. Available: https://www.whitehouse.gov/briefing-room/statements-releases/2023/04/17/fact-sheet-biden-harris-administration-announces-new-private-and-public-sector-investments-for-affordable-electric-vehicles/

[3] 2020. [Online]. Available: https://www.gov.cn/xinwen/2020-11/02/content_5556762.htm

[4] 2023. [Online]. Available: https://www.statista.com/outlook/mmo/electric-vehicles/worldwide#unit-sales

[5] L. Xue, "GaN-based high-efficiency, high-density, high-frequency battery charger for plug-in hybrid electric vehicle," Bradley Dept. Elect. Comput. Eng., Virginia Tech, Blacksburg, VA, USA, 2015.

[6] B. Li, Q. Li, F. C. Lee, Z. Liu, and Y. Yang, "A high-efficiency high-density wide-bandgap device-based bidirectional on-board charger," *IEEE J. Emerg. Sel. Topics Power Electron.*, vol. 6, no. 3, pp. 1627–1636, Sep. 2018.

[7] S. A. Assadi, H. Matsumoto, M. Moshirvaziri, M. Nasr, M. S. Zaman, and O. Trescases, "Active saturation mitigation in high-density dual-active-bridge DC–DC converter for on-board EV charger applications," *IEEE Trans. Power Electron.*, vol. 35, no. 4, pp. 4376–4387, Apr. 2020.

[8] J. Yuan, L. Dorn-Gomba, A. D. Callegaro, J. Reimers, and A. Emadi, "A review of bidirectional on-board chargers for electric vehicles," *IEEE Access*, vol. 9, pp. 51501–51518, 2021.

[9] P. H. Pham, A. Nabih, S. Wang, and Q. Li, "11-kW high-frequency high-density bidirectional OBC with PCB winding magnetic design," in *Proc. IEEE Appl. Power Electron. Conf. Expo.*, 2022, pp. 1176–1181.

[10] S. R. Meher and R. K. Singh, "A standard two stage on-board charger with single controlled PWM and minimum switch count," *IEEE Trans. Ind. Appl.*, vol. 59, no. 4, pp. 4628–4639, Jul./Aug. 2023.

[11] B. Su, J. Zhang, and Z. Lu, "Totem-pole boost bridgeless PFC rectifier with simple zero-current detection and full-range ZVS operating at the boundary of DCM/CCM," *IEEE Trans. Power Electron.*, vol. 26, no. 2, pp. 427–435, Feb. 2011.

[12] Z. Liu, X. Huang, M. Mu, Y. Yang, F. C. Lee, and Q. Li, "Design and evaluation of GaN-based dual-phase interleaved MHz critical mode PFC converter," in *Proc. IEEE Energy Convers. Congr. Expo.*, 2014, pp. 611–616.

[13] Y. Li et al., "Optimal synergetic operation and experimental evaluation of an ultra-compact GaN-based three-phase 10 kW EV charger," *IEEE Trans. Transp. Electrific.*, to be published, doi: 10.1109/TTE.2023.3297502.

[14] D. Zhang, J. Huber, and J. W. Kolar, "A three-phase synergetically controlled buck-boost current DC-link EV charger," *IEEE Trans. Power Electron.*, vol. 38, no. 12, pp. 15184–15198, Dec. 2023.

[15] Z. Huang, G. Son, Q. Li, and F. C. Lee, "Balance techniques and PCB winding magnetics for common-mode EMI noise reduction in three-phase AC–DC converters," *IEEE Trans. Power Electron.*, vol. 37, no. 3, pp. 3130–3142, Mar. 2022.

[16] Y. Cao and D. Dong, "Electronic-embedded transformer based DC transformer with trapezoidal current and natural current sharing," *IEEE Trans. Power Electron.*, vol. 38, no. 10, pp. 12348–12354, Oct. 2023, doi: 10.1109/TPEL.2023.3295130.

[17] Y. Cao, K. Ngo, and D. Dong, "A scalable electronic-embedded transformer—A new concept toward ultra-high-frequency high-power transformer in DC–DC converters," *IEEE Trans. Power Electron.*, vol. 38, no. 8, pp. 9278–9293, Aug. 2023, doi: 10.1109/TPEL.2023.3279259.

[18] H. Bai and C. Mi, "Eliminate reactive power and increase system efficiency of isolated bidirectional dual-active-bridge DC–DC converters using novel dual-phase-shift control," *IEEE Trans. Power Electron.*, vol. 23, no. 6, pp. 2905–2914, Nov. 2008.

[19] A. K. Jain and R. Ayyanar, "PWM control of dual active bridge: Comprehensive analysis and experimental verification," *IEEE Trans. Power Electron.*, vol. 26, no. 4, pp. 1215–1227, Apr. 2011.

[20] F. Jin, A. Nabih, Z. Li, and Q. Li, "A scalable matrix integrated transformer with controllable leakage inductance for a bi-directional resonant converter," *IEEE Trans. Power Electron.*, vol. 38, no. 9, pp. 10967–10984, Sep. 2023.

[21] B. Li, Q. Li, and F. Lee, "High-frequency PCB winding transformer with integrated inductors for a bi-directional resonant converter," *IEEE Trans. Power Electron.*, vol. 34, no. 7, pp. 6123–6135, Jul. 2019.

[22] B. Li, Q. Li, and F. C. Lee, "A WBG based three phase 12.5 kW 500 kHz CLLC resonant converter with integrated PCB winding transformer," in *Proc. IEEE Appl. Power Electron. Conf. Expo.*, 2018, pp. 469–475.

[23] Y. Cao, M. Ngo, N. Yan, D. Dong, R. Burgos, and A. Ismail, "Design and implementation of an 18-kW 500-kHz 98.8% efficiency high-density battery charger with partial power processing," *IEEE J. Emerg. Sel. Topics Power Electron.*, vol. 10, no. 6, pp. 7963–7975, Dec. 2022.

[24] Y. Cao, M. Ngo, R. Burgos, A. Ismail, and D. Dong, "Switching transition analysis and optimization for bidirectional CLLC resonant DC transformer," *IEEE Trans. Power Electron.*, vol. 37, no. 4, pp. 3786–3800, Apr. 2022, doi: 10.1109/TPEL.2021.3125265.

[25] Z. Li, E. Hsieh, Q. Li, and F. C. Lee, "High-frequency transformer design with medium-voltage insulation for resonant converter in solid-state transformer," *IEEE Trans. Power Electron.*, vol. 38, no. 8, pp. 9917–9932, Aug. 2023, doi: 10.1109/TPEL.2023.3279030.

[26] F. Jin, F. Liu, X. Ruan, and X. Meng, "Multi-phase multi-level LLC resonant converter with low voltage stress on the primary-side switches," in *Proc. IEEE Energy Convers. Congr. Expo.*, 2014, pp. 4704–4710, doi: 10.1109/ECCE.2014.6954045.

[27] C. Fei, F. C. Lee, and Q. Li, "High-efficiency high-power-density LLC converter with an integrated planar matrix transformer for high-output current applications," *IEEE Trans. Ind. Electron.*, vol. 64, no. 11, pp. 9072–9082, Nov. 2017.

[28] M. H. Ahmed, A. Nabih, F. C. Lee, and Q. Li, "Low-loss integrated inductor and transformer structure and application in regulated LLC converter for 48-V bus converter," *IEEE J. Emerg. Sel. Topics Power Electron.*, vol. 8, no. 1, pp. 589–600, Mar. 2020, doi: 10.1109/JESTPE.2019.2952878.

[29] A. Nabih and Q. Li, "Design of 98.8% efficient 400-to-48-V LLC converter with optimized matrix transformer and matrix inductor," *IEEE Trans. Power Electron.*, vol. 38, no. 6, pp. 7207–7225, Jun. 2023, doi: 10.1109/TPEL.2023.3244869.

[30] R. Schlesinger and J. Biela, "Comparison of analytical models of transformer leakage inductance: Accuracy versus computational effort," *IEEE Trans. Power Electron.*, vol. 36, no. 1, pp. 146–156, Jan. 2021.

[31] G. Liu, D. Li, J. Q. Zhang, B. Hu, and M. L. Jia, "Bidirectional CLLC resonant DC-DC converter with integrated magnetic for OBCM application," in *Proc. IEEE Int. Conf. Ind. Technol.*, 2015, pp. 946–951, doi: 10.1109/ICIT.2015.7125219.

[32] H. A. Kojori, J. D. Lavers, and S. B. Dewan, "State plane analysis of a resonant DC-DC converter incorporating integrated magnetics," *IEEE Trans. Magn.*, vol. 24, no. 6, pp. 2898–2900, Nov. 1988.

[33] J. Biela and J. W. Kolar, "Electromagnetic integration of high power resonant circuits comprising high leakage inductance transformers," in *Proc. IEEE 35th Annu. Power Electron. Specialists Conf.*, 2004, vol. 6, pp. 4537–4545.

[34] A. Nabih, Q. Li, and F. C. Lee, "Magnetic integration of four-transformer matrix with high controllable leakage inductance using a five-leg magnetic," in *Proc. IEEE Appl. Power Electron. Conf. Expo.*, 2022, pp. 693–700.
[35] A. Nabih, F. Jin, and Q. Li, "Efficient integrated transformer–inductor with high PCB utilization and optimized core," *IEEE Trans. Ind. Electron.*, to be published, doi: 10.1109/TIE.2023.3294637.
[36] R. Gadelrab and F. Lee, "PCB-based magnetic integration and design optimization for three-phase LLC," *IEEE Trans. Power Electron.*, vol. 38, no. 11, pp. 14037–14049, Nov. 2023, doi: 10.1109/TPEL.2023.3285652.
[37] J. Li et al., "Matrix inductor-transformer integration and optimization design for CLLC bidirectional resonant converter," *Proc. CSEE*, vol. 42, no. 10, pp. 3720–3729, May 2022.
[38] Y. Liu, H. Wu, Z. Ge, and G. Ji, "Magnetic integration for multiple resonant converters," *IEEE Trans. Ind. Electron.*, vol. 70, no. 8, pp. 7604–7614, Aug. 2023, doi: 10.1109/TIE.2022.3229381.
[39] X. Chen, G. Xu, Q. Shen, Y. Sun, and M. Su, "Magnetizing and leakage inductance integration for split transformers with standard UI cores," *IEEE Trans. Power Electron.*, vol. 37, no. 11, pp. 12980–12985, Nov. 2022.
[40] Z. Li, F. Jin, C. Zhao, E. Hsieh, and Q. Li, "A high-frequency transformer design with leakage integration for auxiliary power supply in railway application," in *Proc. 11th Int. Conf. Power Electron. ECCE Asia*, 2023, pp. 3402–3409.
[41] T. Yuan, F. Jin, Z. Li, C. Zhao, and Q. Li, "Design of an integrated transformer with parallel windings for a 30-kW LLC resonant converter," *IEEE Trans. Power Electron.*, vol. 38, no. 11, pp. 14317–14333, Nov. 2023, doi: 10.1109/TPEL.2023.3291954.
[42] F. Jin, A. Nabih, Q. Li, and F. C. Lee, "A three phase CLLC converter with improved planar integrated transformer for fast charger applications," in *Proc. IEEE 4th Int. Conf. DC Microgrids*, 2021, pp. 1–5, doi: 10.1109/ICDCM50975.2021.9504644.
[43] P. L. Dowell, "Effects of eddy currents in transformer windings," *Proc. IEE*, vol. 113, pp. 1387–1394, 1966.
[44] J. A. Ferreira, "Improved analytical modeling of conductive losses in magnetic components," *IEEE Trans. Power Electron.*, vol. 9, no. 1, pp. 127–131, Jan. 1994.
[45] A. Nabih, F. Jin, R. Gadelrab, F. C. Lee, and Q. Li, "Characterization and mitigation of dimensional effects on core loss in high-power high-frequency converters," *IEEE Trans. Power Electron.*, vol. 38, no. 11, pp. 14017–14036, Nov. 2023, doi: 10.1109/TPEL.2023.3285633.
[46] J.-W. Kim and P. Barbosa, "PWM-controlled series resonant converter for universal electric vehicle charger," *IEEE Trans. Power Electron.*, vol. 36, no. 12, pp. 13578–13588, Dec. 2021.
[47] S. Mukherjee, J. M. Ruiz, and P. Barbosa, "A high power density wide range DC–DC converter for universal electric vehicle charging," *IEEE Trans. Power Electron.*, vol. 38, no. 2, pp. 1998–2012, Feb. 2023, doi: 10.1109/TPEL.2022.3217092.
[48] L. A. D. Ta, N. D. Dao, and D.-C. Lee, "High-efficiency hybrid LLC resonant converter for on-board chargers of plug-in electric vehicles," *IEEE Trans. Power Electron.*, vol. 35, no. 8, pp. 8324–8334, Aug. 2020.
[49] Y. Park, S. Chakraborty, and A. Khaligh, "DAB converter for EV onboard chargers using bare-die SiC MOSFETs and leakage-integrated planar transformer," *IEEE Trans. Transp. Electrific.*, vol. 8, no. 1, pp. 209–224, Mar. 2022.
[50] H. Li et al., "A bidirectional synchronous/asynchronous rectifier control for wide battery voltage range in SiC bidirectional LLC chargers," *IEEE Trans. Power Electron.*, vol. 37, no. 5, pp. 6090–6101, May 2022.
[51] S. Mukherjee and P. Barbosa, "Design and optimization of an integrated resonant inductor with high-frequency transformer for wide gain range DC–DC resonant converters in electric vehicle charging applications," *IEEE Trans. Power Electron.*, vol. 38, no. 5, pp. 6380–6394, May 2023, doi: 10.1109/TPEL.2023.3243807.
[52] G. Liu, Y. Jang, M. M. Jovanovic, and J. Q. Zhang, "Implementation of a 3.3-kW DC-DC converter for EV on-board charger employing series-resonant converter with reduced-frequency-range control," *IEEE Trans. Power Electron.*, vol. 32, no. 6, pp. 4168–4184, Jun. 2017.
[53] G. Wei, H. Bai, G. Szatmari-Voicu, A. Taylor, J. Patterson, and J. Kane, "A 10kW 97%-efficiency LLC resonant DC/DC converter with wide range of output voltage for the battery chargers in plug-in hybrid electric vehicles," in *Proc. IEEE Transp. Electrific. Conf. Expo.*, 2012, pp. 1–4.
[54] G. Yang, E. Draugedalen, T. Sorsdahl, H. Liu, and R. Lindseth, "Design of high efficiency high power density 10.5kW three phase on-board-charger for electric/hybrid vehicles," in *Proc. Int. Exhib. Conf. Power Electron., Intell. Motion, Renewable Energy Energy Manage.*, 2016, pp. 1–7.
[55] J. Schmenger, S. Endres, S. Zeltner, and M. März, "A 22 kW on-board charger for automotive applications based on a modular design," in *Proc. IEEE Conf. Energy Convers.*, 2014, pp. 1–6.

Feng Jin (Graduate Student Member, IEEE) received the B.Sc. and M.Sc. degrees in electrical engineering from the Nanjing University of Aeronautics and Astronautics, Nanjing, China, in 2012 and 2015, respectively. He is currently working toward the Ph.D. degree in electrical engineering with the Center for Power Electronics Systems, Virginia Tech, Blacksburg, VA, USA.

From 2015 to 2019, he was an Electrical Engineer with Delta Electronics, Hangzhou, China. He participated in the development of power supply units for server/telecom applications with Delta Electronics. His current research interests include EV charging, bidirectional power conversion, and planar magnetics.

Mr. Jin was the recipient of the Best Presentation Award at the IEEE Applied Power Electronics Conference and Exposition in 2023.

Ahmed Nabih (Member, IEEE) received the B.Sc. and M.Sc. degrees from Cairo University, Giza, Egypt, in 2014 and 2017, respectively, and the Ph.D. degree from Virginia Tech, Blacksburg, VA, USA, in 2023, all in electrical engineering.

He is currently a System Engineer with Texas Instruments, Inc., Dallas, TX, USA. His research interests include wide bandgap technology, high-power drivers, digital control, high-frequency resonant converter design, and planar magnetics.

Dr. Nabih was the recipient of the Best Paper Award of the OCP Future Technology Symposium in 2020 and multiple APEC outstanding presentation awards.

Tianlong Yuan (Graduate Student Member, IEEE) received the B.S. degree in electrical engineering from the Harbin Institute of Technology, Harbin, China, in 2019. He is currently working toward the Ph.D. degree in electrical engineering with the Center for Power Electronics Systems, Virginia Tech, Blacksburg, VA, USA.

His research interests include EV charging, bidirectional power conversion, and integrated planar magnetics.

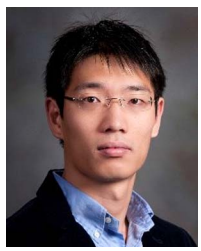

Qiang Li (Member, IEEE) received the B.S. and M.S. degrees in power electronics from Zhejiang University, Hangzhou, China, in 2003 and 2006, respectively, and the Ph.D. degree in electrical engineering from Virginia Tech, Blacksburg, VA, USA, in 2011.

He is currently a Professor with the Center for Power Electronics Systems, Virginia Tech. He holds 37 U.S. patents and has authored or coauthored more than 200 refereed technical articles. His research interests include power management for distributed power systems, applications of wide-bandgap power devices, high-frequency power conversion and controls, magnetics and electromagnetic interference, high-density electronics packaging and integration, and renewable energy.

Dr. Li was the recipient of the First Place Prize Article Award of IEEE Transactions on Power Electronics in 2016 and the 2017 U.S. National Science Foundation Career Award.